A comparative study of commercial lithium ion battery cycle life in electrical vehicle: Aging mechanism identification

Xuebing Han, Minggao Ouyang*, Languang Lu, Jianqiu Li, Yuejiu Zheng, Zhe Li

Department of Automotive Engineering, State Key Laboratory of Automotive Safety and Energy, Tsinghua University, Beijing 100084, PR China

HIGHLIGHTS

- Aging mechanisms of five different battery types are analyzed by incremental capacity curve.
- Aging mechanisms of LFP batteries are analyzed by charging voltage curve reproduction.
- On-line identification of aging mechanism and SOH estimation of LFP batteries are discussed.

ARTICLE INFO

ABSTRACT

When lithium-ion batteries age with cycling, the battery capacity decreases and the resistance increases. The aging mechanism of different types of lithium-ion batteries differs. The loss of lithium inventory, loss of active material, and the increase in resistance may result in battery aging. Generally, analysis of the battery aging mechanism requires dismantling of batteries and using methods such as X-ray diffraction and scanning electron microscopy. These methods may permanently damage the battery. Therefore, the methods are inappropriate for the battery management system (BMS) in an electric vehicle. The constant current charging curves while charging the battery could be used to get the incremental capacity and differential voltage curves for identifying the aging mechanism; the battery state-of-health can then be estimated. This method can be potentially used in the BMS for online diagnostic and prognostic services. The genetic algorithm could be used to quantitatively analyze the battery aging offline. And the membership function could be used for onboard aging mechanism identification.

© 2013 Elsevier B.V. All rights reserved.

1. Introduction

Owing to the energy crisis and the adverse environmental effects of hydrocarbon-based transport, there has been significant development of electric vehicles (EVs) over the last decades, especially the pure EVs in which batteries are among the most critical parts. Lithium-ion batteries are currently widely developed for vehicle applications owing to their high energy and power densities, long life, and lack of memory effect.

Presently, in order to improve the performance of EV, it is important to improve the battery systems by both manufacturing better performing cells and developing better battery management system (BMS). State estimation, mainly containing state-of-charge (SOC), state-of-health (SOH), state-of-function (SOF), and state-of-safety (SOS), is one of the most critical functions of the BMS. SOH is one of the most important battery state parameters for the BMS to reasonably estimate battery performance and for the vehicle control unit to reasonably use batteries [1].

However, at present, SOH estimation is generally limited to estimation of only certain battery parameters, for example, battery capacity estimation or resistance identification, and analysis of the deviation from the performance of a new battery. Such simple data cannot meet the requirement of a BMS to identify the actual conditions inside the batteries, and thus identification of the battery aging mechanism is needed.

The aging mechanism and cycle life of different types of batteries are obviously different and mainly depend on the cathode and anode material type. At present, cathode materials for commercial lithium-ion batteries include LiFePO$_4$ (LFP), LiMn$_2$O$_4$ (LMO), and LiNi$_x$Co$_y$Mn$_{1-x-y}$O$_2$ (NCM), and anode materials include Li$_4$Ti$_5$O$_{12}$ (LTO) and graphite (C). Batteries of different electrode materials differ in performance, especially in cycle life.

Furthermore, battery aging can arise from many factors such as loss of lithium inventory (LLI), loss of active material (LAM), and

* Corresponding author. Tel.: +86 10 62792797; fax: +86 10 62789699.
 E-mail addresses: ouymg@tsinghua.edu.cn, coldsnowicer@gmail.com (M. Ouyang).

increase in resistance [2]. The battery SOH estimation limited to changes in the available capacity does not sufficiently reflect battery health. Therefore, it is necessary to analyze whether the internal mechanism causing capacity changes arise from LLI or LAM. This will enable comprehensive analysis of battery aging for better diagnosis of battery degradation and SOH estimation, thereby facilitating prediction of future battery aging. In some cases, power batteries are used in vehicles until their performance degrades to an extent to which they fail to meet the energy demands of the vehicle, and then they can be sold to power storage stations for reuse [3]. Then explore the aging mechanism of batteries would optimize the usage of batteries and extend their lifetimes.

Generally, investigation of battery aging mechanisms requires dismantling and destroying of batteries and using methods such as X-ray diffraction (XRD) and scanning electron microscopy (SEM). However, these techniques involve destruction of batteries and complicated equipment, thus cannot be applied to the BMS of a vehicle. Hence, in situ voltage measurement methods are necessary. During the slow charging process of EV, the incremental capacity (IC) curves (dQ/dV) and differential voltage (DV) curves (dV/dQ) can be derived by the battery constant current charge curves. From the IC and DV curves, more information can be determined than from the charge and discharge curves alone. Thus, from the changes in the IC or DV curves, the internal changes in batteries over their lifetime (as a function of increasing cycle number) can be analyzed. From this, the predominant aging mechanism degrading battery performance can be investigated. Dubarry et al. introduced and validated the IC analysis [2,32,33]. The methods involving DV was introduced by Bloom et al. [4]; Honkura et al. [5]; and Dahn et al. [6]. These methods have the potential for achieving online battery diagnosis with the BMS.

Note that this paper does not focus on the battery aging mechanism study. There are many factors and mechanisms causing battery aging; this study primarily used the IC and DV curves to study the performance before and after cycling of several lithium-ion batteries suitable for EVs. We referred to the studies of Dubarry et al. [2] and Bloom et al. [4] to explore how to identify the aging mechanisms and estimate the SOH in electric vehicle.

In this study, five types of commercial lithium-ion batteries were tested and compared. The basic parameters of the five types of batteries are shown in Table 1. For convenience, these five types of batteries are labeled as cells A, B, C, D, and E.

The batteries were charged at 1/3 C, discharged at 1.5 C, 90 cycles under 45 °C, and 90 cycles under 5 °C; after every 30 cycles, a reference performance test (RPT) was conducted. The results of the RPT are shown in Fig. 1. The last charge curve was used to calculate the IC and DV curves.

In Section 2, a brief summary of the aging mechanism of common commercial lithium-ion batteries is introduced along with a simple model for practical use. In Section 3, the aging mechanism of LFP batteries, which have been currently much researched, is shown. Section 4 presents the aging mechanism of LMO batteries. Section 5 presents an analysis of the aging mechanism of LTO batteries. Conclusions of the study are presented in the final section.

Table 1
Basic parameters of the five types of batteries.

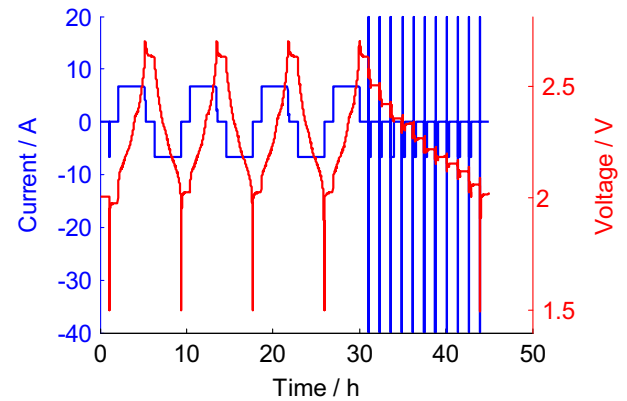|	Battery type	Rated capacity (Ah)	Rated voltage (V)	Weight (kg)
A	LTO/NCM	20	2.3	0.510
B	C/LFP	60	3.2	2.5
C	C/LFP	11	3.2	0.36
D	C/LMO	35	3.7	1.08
E	C/LMO	10	3.7	0.30

Fig. 1. Reference performance test profile.

2. Aging mechanisms of lithium-ion batteries

2.1. Comparison of aging mechanisms of different types of batteries

The aging mechanism of lithium-ion batteries is very complicated. It may depend on the parameters such as cathode and anode materials, preparation methods, electrolyte composition, and battery working conditions. In this section, the battery aging mechanism is briefly discussed with respect to the cathode and anode of lithium-ion batteries [15].

At present, the anode material for commercial lithium-ion batteries is usually graphite. For example, the anode of cells B, C, D, and E is all graphite based material. As shown in Fig. 2 (adapted from [9] and [10]), common liquid organic electrolytes have a stabilized voltage window of 0.8–4.5 V, and the graphite anode works at a voltage of approximately 0.05 V [9], which is beyond the stabilized voltage window of electrolytes. Thus, in theory, the graphite anode of lithium-ion batteries is unstable thermodynamically. However, loss of lithium ions will occur along with electrolyte decomposition during the charge–discharge process of batteries, thereby forming a passivation protective layer, i.e., a solid electrolyte interface (SEI) film [11], on the surface of graphite anode. Under ideal conditions, the SEI film only transports lithium ions and not electrons so as to prevent further electrolyte degradation. Thus, lithium-ion batteries with graphite anodes can be cycled and stay stable [12–14]. This SEI
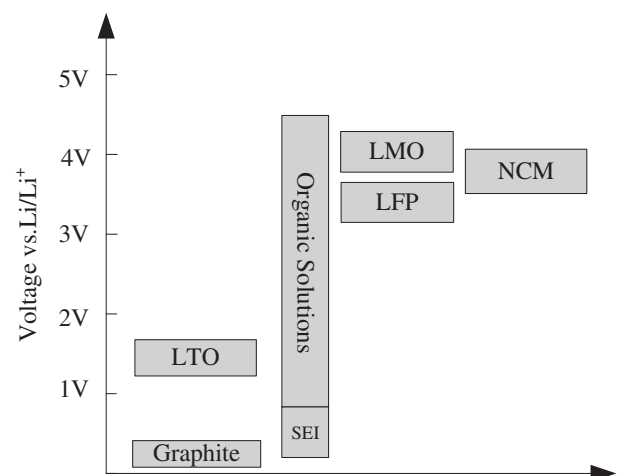

Fig. 2. Voltage vs. Li/Li$^+$ of the electrode materials of five types of batteries in comparison with the stability window of common liquid organic electrolytes.

film mainly forms during the first charging process of batteries; thus, the lithium-ion battery capacity rapidly decreases after the first one or several cycles. During battery charging–discharging processes, approximately 10% (or less) volume change can occur in the graphite anode because of the insertion and extraction of lithium ions [15]. As this volume change can cause the SEI film to crack, it is inevitable that lithiated graphite can come into contact and react with the electrolyte solution species for each battery cycle, and thus the electrolyte and lithium inventory are consumed continuously [13,14,16]. This leads to continuous decrease in available battery capacity and continuous thickening of the SEI film, thereby resulting in increase in battery resistance. This is widely accepted as one of the major reasons for lithium-ion battery aging. Besides, while charging at low temperature or with a high charge rate, there may be metallic lithium plating and subsequent electrolyte decomposition by metallic Li on the graphite surface, again leading to loss of electrolyte and lithium inventory [15]. In addition, the volume change may lead to contact loss with active material particles [14]. Co-intercalation of Li ions with solvent molecules may lead to exfoliation of the graphite particles [15]. There may also be corrosion of current collectors and adhesives. These phenomena may also lead to decrease in battery capacity.

The spinel lithium titanium oxides (LTO) are a new generation of lithium-ion battery anode material found in recent years. As their electric potentials are within the stabilized window of electrolytes (approximately 1.55 V vs. Li/Li$^+$ [10]), there would be no SEI film production. Owing to the high electric potential, there would be no reduction in ions such as Li$^+$ and Mn^{2+}, and thus no metal deposition. In addition, LTO is a zero-strain material, which means that there is no structural and almost no volume change during the insertion and extraction of lithium ions [10,17,18]; hence, the LTO materials have excellent durability. LTO anodes also have excellent low-temperature performance and high C-rate charge–discharge performance. The high electric potential of LTO anodes leads to a lower voltage of lithium-ion batteries with these anodes than with a graphite anode with the same cathode material, resulting in some reduction in the battery energy density. However, considering the long cycle life and high thermal stability, LTO is currently regarded as one of the most promising anode materials for lithium-ion power batteries for vehicles and may substitute graphite for mass production. For example, in this study Cell A with LTO anodes apparently shows a lower capacity fade rate than cells B, C, D, and E with graphite anodes for the same cycles.

At present, the cathode materials of commercial lithium-ion batteries mainly include LMO, LFP, and NCM (mainly LiNi$_{1/3}$Co$_{1/3}$Mn$_{1/3}$O$_2$, namely L333), as the five cells tested here.

The spinel lithium manganese oxides (LMO) used as cathodes are nontoxic with high energy density and low price and are currently among the electrode materials receiving wide attention. Two of the main reasons for the aging of LMO are the structural deformation caused by Mn^{3+} Jahn–Teller distortion and dissolution of Mn^{2+} in electrolytes [15,19]. In LMO cathode, Mn is usually present in two oxidation states Mn^{3+} and Mn^{4+}. While discharging to a lower potential, especially at high rates, because lithium ions have much faster diffusion rates in electrolytes than in LMO particles during discharging, lithium ions accumulate on the surface of LMO particles and additional lithium ions are inserted. Thus, reduction of Mn^{4+} to Mn^{3+} occurs, and Jahn–Teller distortion is induced, which leads to a phase transition from cubic to tetragonal, resulting in approximately 16% volume change of LMO [20–22] and hence capacity fade. The dissolution of Mn^{2+} may be caused by Mn^{3+} disproportionating into Mn^{2+} and Mn^{4+} where Mn^{2+} can dissolve in electrolytes [23] or by acid dissolution catalyzed by HF, and insoluble LiF may be generated on the electrode surface [15,24]. The dissolution of Mn^{2+} results in the LAM and electrolytes as well

as structural damage to the cathode. For batteries with a graphite anode, the Mn^{2+} ions may move to the anode and be reduced on the surface because of the lower potential of the graphite anode; the ions catalyze the thickening of the SEI film [15,24], leading to a continuous battery capacity fade and increase in resistance. For example, the capacity fade rates of LMO cells D and E in this study are far higher than those of other types of cells. In contrast, since the LTO anode with a higher electrical potential has direct contact with the electrolyte and no SEI film formation or Mn ion reduction occurs, the lithium-ion batteries with an LMO cathode and LTO anode would have a much longer battery cycle life than those with LMO cathodes and graphite anodes [25].

Layered LiNi$_x$Co$_y$Mn$_{1-x-y}$O$_2$ is currently receiving much attention owing to its high energy density, long cycle life and calendar life, high reliability, and low price. The volume change is only approximately 2% during insertion and extraction of lithium ions [26]. Cell A with an LTO anode and NCM cathode shows a very long cycle life and almost no capacity fade. The capacity loss of NCM is mainly caused by (1) changes in lattice volume during charge or discharge; (2) cation mixing; (3) transition metal ion dissolution; (4) side reactions between electrode and electrolyte [27,28].

The olivine LiFePO$_4$ anode has low energy density because of its low voltage and high resistance; however, it also has very long cycle life and calendar life, low price, and good thermal stability. During cycling, the volume change is only approximately 6.77% [29]. The Fe^{2+} ions are relatively stable; however, similar to LMO, the electrolyte may also dissolve Fe ions, resulting in loss of the cathode active material. The Fe ions may also reduce on the surface of the graphite anode and catalyze the SEI formation, thereby leading to increase in resistance and loss of Li ions [29]. However, compared with LMO batteries, the cycle life of LFP cells is much longer, for example, in this experiment, the LFP cells B and C show much lower capacity fade rates than the LMO cells D and E. In addition, batteries with an LFP cathode and LTO anode will have very low voltage, with a very low energy density but a very long cycle life [30].

2.2. Tank model and battery aging mechanism classification

According to the literature [39], our comprehension about lithium-ion batteries and the potential application in a BMS, we use a simple tank model, as shown in Fig. 3, as an analogy of lithium-ion batteries. A similar water-clock model has been shown in the literature [39]. Specifically, the cathode and anode of the battery are
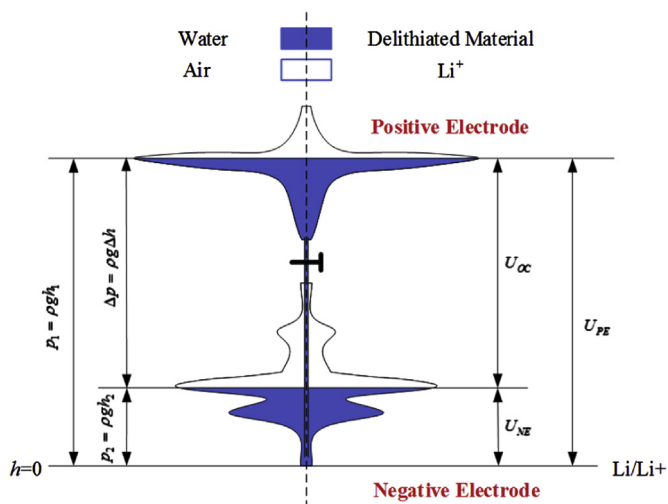

Fig. 3. Water tank model.

equivalent to two tanks, which may have complex shapes. Lithium ions are similar to water in the tanks. In the case of real water tanks, more water in the tank corresponds to a higher water level and higher pressure. However, for almost all of the lithium-ion battery electrode materials, a higher density of lithium ions corresponds to a lower electrical potential. When charging the batteries, it may be considered that lithium ions move from the cathode to the anode, where the lithium density of the cathode decreases and that of the anode increases. Conversely, when discharging the batteries, the lithium ions move from the anode to the cathode. Such a process is similar to the exchange of water between the two tanks. The capacity of batteries manifests the number of lithium ions exchanged between the cathode and the anodes in the aforesaid exchange process. For tanks, the volume of water exchanged depends on the size of the two tanks and the volume of available water. Therefore, the aging mechanism of this entire tank system is related to the loss of available water and the capacity loss of the two tanks.

Similarly, the aging mechanism of batteries can be roughly divided into the following types: LLI and LAM. In addition, batteries can suffer from increasing resistance, which mainly includes Ohmic resistance. LLI mainly arises from the formation of SEI film, lithium plating, etc. Therefore, it is more likely to occur in batteries with graphite anodes. There is a smaller effect of LLI on batteries with LTO anodes. LAM is mainly a result of structural damage and material loss arising from dissolution of Mn and Fe ions. Graphite anodes and LMO cathodes are likely to suffer LAM. LFP and NCM cathodes can be subjected to LAM but to a much lesser extent than LMO cathodes. LTO anodes may suffer less LAM. Increase in resistance mainly arises from loss of electrolytes, contact resistance, and SEI film resistance.

In the literature [2], LAM effects are further divided into four types of aging mechanisms: (1) loss of lithiated cathode, (2) loss of delithiated cathode, (3) loss of lithiated anode, and (4) loss of delithiated anode materials. For simplification, we only consider LAM as loss of cathode or anode material. The loss of lithiated cathode material, for example, is considered as a combination of the loss of cathode material and LLI.

2.3. Incremental capacity curve

In Fig. 3, it can be seen that the sectional area A of the water tank at different height is not constant; in other words, the water pressure change dp differs at different heights h by adding water quantity dQ.

Generally speaking, water pressure and water height conform to Eq. (1).

$$p = \rho g h, \tag{1}$$

where ρ and g are the constants of water density and gravity, respectively.

$$dp = \rho g dh = \rho g \frac{dQ}{A} \tag{2}$$

this means

$$\frac{dQ}{dp} = A/\rho g. \tag{3}$$

Hence, according to dQ/dp, the sectional area at different heights can be calculated, and the condition of this tank system can be known.

Similarly, dQ/dV–V curves (i.e. IC curves) could be used to investigate the conditions of the cathode and anode inside lithium-ion batteries, and then the aging mechanism could be derived. Such curves are named IC curves. In addition, dV/dQ–Q curves, i.e., DV curves, could be used for analyzing the battery aging mechanism as well. The peaks of IC curves, representing the process of phase transformation [2,31–33], correspond to the valleys of DV curves. The peaks of DV curves basically represent the point at which the battery electrode material gets into a certain single phase. The distance between two peaks in a DV curve represents the capacity of a phase transformation involved in the two phases.

In most cases, IC or DV curves are obtained by charging or discharging the battery by means of very small current such as 1/25 C in order to ensure that the batteries operate under an approximate equilibrium (static) state [2]. However, time restrictions in the process of actual on-board use in a vehicle indicate that the battery charging current will generally be larger than this. Therefore, the IC and DV curves mentioned in this study are obtained by means of 1/3 C charge curves. The reason for using charge curves instead of discharge curves mainly lies in the fact that for EVs, the discharging process tends to be relatively dynamic which depends on the driving cycles, and the charging process tends to be completed in a charging station or at home by constant current charging. However, constant current discharge curves are probably available from the process of regular maintenance of batteries; thus, the BMS can also possibly obtain constant current discharge curves. However, it is more convenient for the BMS to obtain constant current charge curves. Better results would be expected using micro currents to charge or discharge batteries to obtain IC and DV curves, and more accurate understanding of the aging mechanism could be derived. However, in this study, we aimed to determine a method for identifying the SOH and the aging mechanism of batteries for the BMS in the vehicle. Thus, 1/3C constant-current charging curves are used for analysis.

A method of obtaining IC curves based on the probability density function has been introduced in our previous paper [34]. Here we only give a brief introduction to an equivalent point counting method for IC curves, and the theoretical inference will not be repeated.

Considering the LFP cell, the terminal voltage of LFP batteries increases from the minimum 2.5 V (depending on the discharging process) to 3.6 V in the process of constant current charging. This range is divided into several small intervals. During the charging process, the battery voltage was measured, and the number of voltage points within each interval was recorded. Generally, the battery is charged at constant current, and the voltage sampling frequency of the BMS is constant, usually 1 Hz. Thus, the charged battery capacity is proportional to the number of sampling points in the charging process. In other words, when the voltage increases at a higher rate, there are fewer points in the corresponding voltage interval, and when the voltage increases at a lower rate (i.e., a voltage plateau occurs), there are more points in the corresponding voltage interval. The dQ/dV can be calculated using Eq. (4).

$$\frac{dQ}{dV} = \frac{nI}{3600 f \Delta V} \tag{4}$$

Here n is the number of points counted in the corresponding interval. I is the charging current (A), and f is the sampling frequency (Hz). ΔV is the width of each voltage interval (V). A voltage interval width of 5 mV was selected. Curve smoothing and filtering are required in order to remove noise.

The DV curves could be obtained by means of a numerical derivative and curve smoothing.

3. Analysis of LFP battery aging mechanism

3.1. IC and DV Curves

Many studies have been reported [2,32,33,35,36] on analysis of the aging mechanism of LFP batteries using the IC and DV curves. This method has the potential to be integrated in a BMS to estimate the battery SOH and observe the internal changes in batteries in real time.

Fig. 4 shows the changes in potential vs. Li/Li+ in LFP cathode and graphite anode during the charging process as well as the measured terminal voltage of C/LFP cell B. The potential of the cathode and the anode is referred to in the literature [37]. It can be easily determined that with the insertion and extraction of lithium ions, the cathode material gradually transforms from $FePO_4$ into $LiFePO_4$ or vice versa, and such a $FePO_4$–$LiFePO_4$ (LFP) phase transformation corresponds to a voltage plateau. During the battery charging or discharging process, the cathode is primarily on this voltage plateau, thereby providing a reference potential for the anode reaction. This phase transformation region of the cathode is marked as II. For the anode, with the insertion and extraction of lithium ions, the electrode material gradually transforms from C into LiC_6 or vice versa. There are three obvious voltage plateaus; each voltage plateau corresponds to a phase transformation process of graphite anode, and the three corresponding phase transformation processes are denoted as ①, ②, and ⑤, respectively. There are three obvious voltage plateaus on the charging voltage curves of the whole batteries, corresponding to the three-phase transformation processes of the graphite anode and the one-phase transformation process of the cathode. These three plateaus
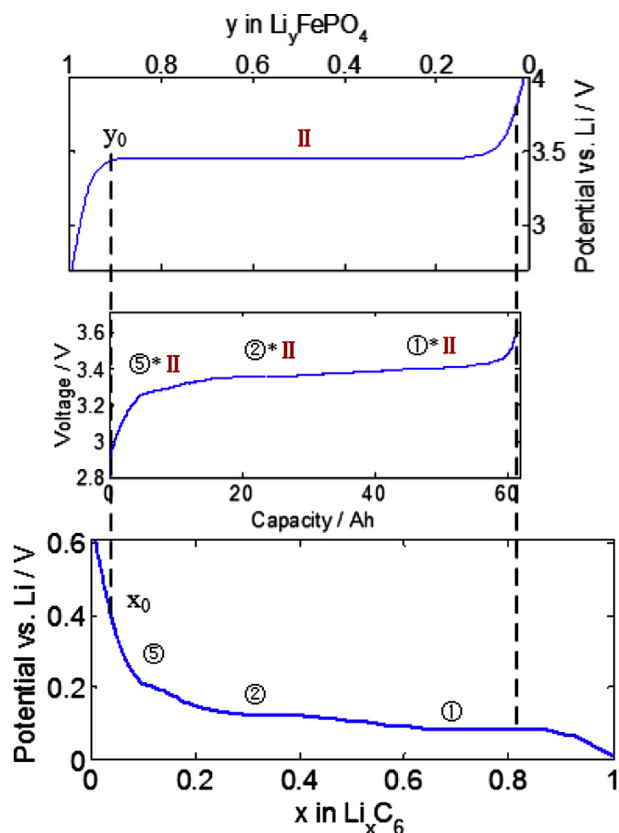
are denoted as ① *II, ② *II and ⑤*II, with reference to the literature [2,32,39].

Battery IC curves could be determined on the basis of the constant current charge curves using the method described in Section 2.3. The charge voltage curve and IC curve of C/LFP cell B are shown in Fig. 5. The three peaks of the obtained IC curve correspond to the three plateaus of the battery charge curve, or rather, correspond to the three voltage plateaus of the graphite anode, as shown in Fig. 5 [35]. A study [32] considered that there are at least five plateaus for the graphite anode; thus, five corresponding peaks on the IC curves of batteries are composed of LFP cathode and graphite anode. Two additional peaks could be found between Peaks ② *II and ⑤*II in Fig. 5 but not obvious.

The IC curves of fresh C/LFP cells B and C are shown in Fig. 6. The IC curves of these two LFP cells from different manufactures are quite similar, and it is convenient to identify the three peaks. The area under each peak represents the capacity involved in the related reaction. The battery aging mechanism can be identified by analyzing the changes in each peak with an increasing number of cycles.

In Fig. 7, the IC curves of new batteries and batteries after various cycles are compared. For C/LFP cell C, only the peak corresponding to ① *II degrades (Fig. 7). Peaks ② *II and ⑤ *II do not change in shape or size, showing that there is no obvious loss of anode material of the battery, which otherwise is supposed to be reflected by all the peaks of the IC curve. Besides, the degradation of Peak ① *II is expected to arise from the LLI process [2,32,33]. The positions of each peak do not change, indicating that there is no obvious increase in the battery resistance. Other studies [33,35,36] have made similar conclusions in terms of the durability tests of commercial LFP batteries, i.e., LLI is the major source of battery aging, and there is almost no aging of the cathode or anode material.

In contrast, for C/LFP cell B, all the three peaks significantly degrade, indicating that there is loss of active material, specifically loss of anode material that leads to degradation of the three peaks. The peak corresponding to ① *II degrades more than the peaks corresponding to ② *II and ⑤ *II, indicating that, besides the loss of anode material, there is also LLI similar to C/LFP cell C. All of the peaks of the IC curve shifted to higher voltages, indicating there may be small increase in the battery resistance.

The DV curves may also be used to investigate the internal changes in batteries with their aging. Fig. 8 plots the DV curve obtained from the charge curve of C/LFP cell B. The peaks of the DV curve naturally divide the curve into three regions. The battery
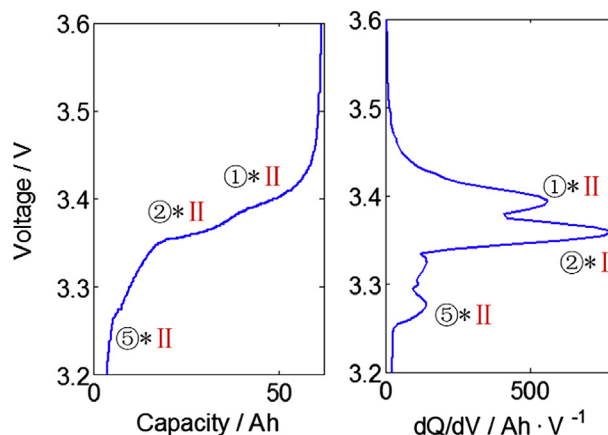

Fig. 4. Potential vs. Li/Li+ of a LFP electrode and graphite electrode, and the voltage of the full C/LFP cell B.

Fig. 5. Cell voltage constant current charge voltage curves and the IC curves of C/LFP cell B.
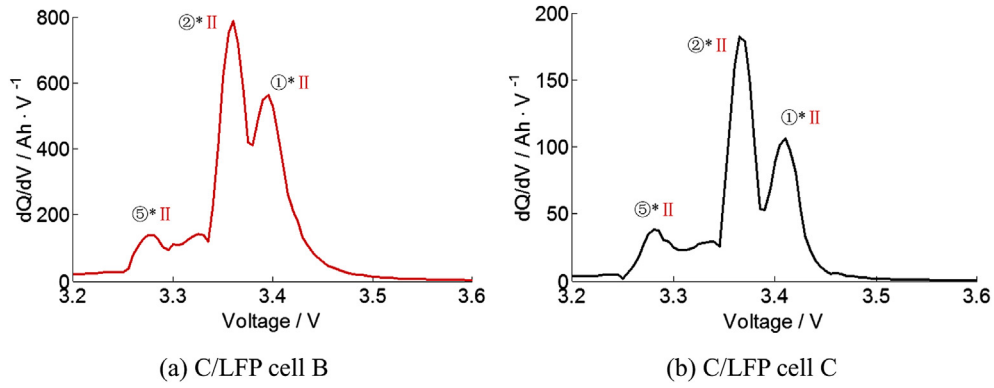
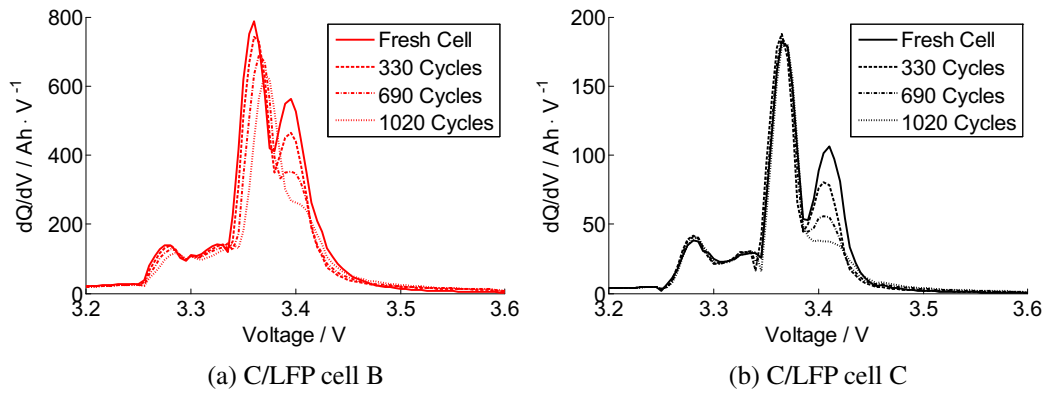**Fig. 6.** IC curves of fresh cell. (a) C/LFP cell B; (b) C/LFP cell C.

Fig. 7. IC curves of full cells after various cycles. (a) C/LFP cell B; (b) C/LFP cell C.
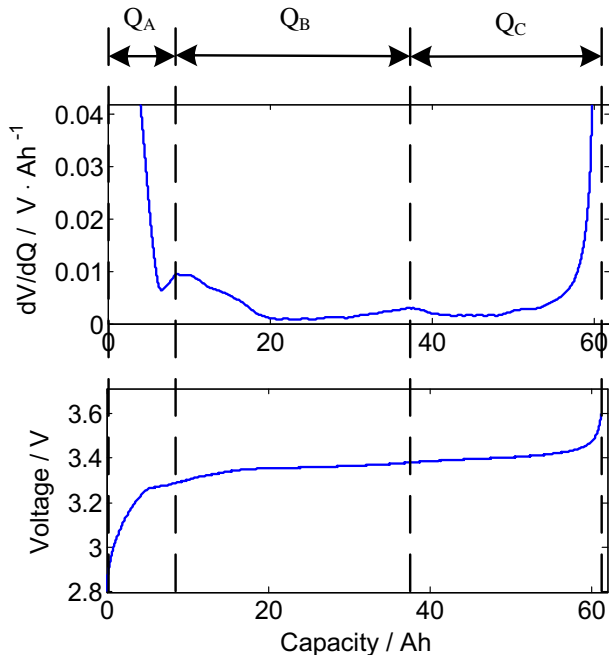

Fig. 8. Differential voltage plot and the cell voltage constant current charge voltage curves (C/LFP cell B).

capacity charges corresponding to each of the aforesaid regions are marked as Q_A, Q_B, and Q_C, which correspond to Fig. 5, can be related to the areas under Peaks ⑤ *II, ② *II, and ① *II on the IC curve, respectively. In short, the aging mechanism of the battery can be similarly investigated by investigating the changes in Q_A, Q_B, and Q_C.

The DV curves of new batteries and after being subjected to a number of cycles are plotted and compared in Fig. 9. Q_A, Q_B, and Q_C of C/LFP cell B significantly decrease as the cycle number increases, indicating there is loss of internal material of the battery and thereby verifying the aforesaid result obtained from the IC curve analysis. Furthermore, Q_A and Q_B of C/LFP cell C do not change significantly, indicating no LAM inside the battery, and Q_C decreases, indicating the capacity loss mainly arises because of LLI.

3.2. Charge curves reconstruction using the genetic algorithm

Analyzing battery aging using IC or DV curves has the potential to be applied to a BMS. The IC or DV curves can be obtained by real-time calculations according to the constant current charge curves in the slow charging process of the battery. The differences in the IC or DV curves between the fresh cell and the current state can identify the internal aging mechanism of batteries in real time and estimate the battery SOH. However, such a method may be available only to qualitatively analyze the battery aging, and it seems quite difficult to perform precise quantitative analysis. As a result, according to the work of Dubarry et al. [2], it is considered to identify the aging of the cathode and anode and semiquantitatively analyze the battery aging through the reconstruction of constant current charge voltage curves according to the potential of cathodes and anodes.
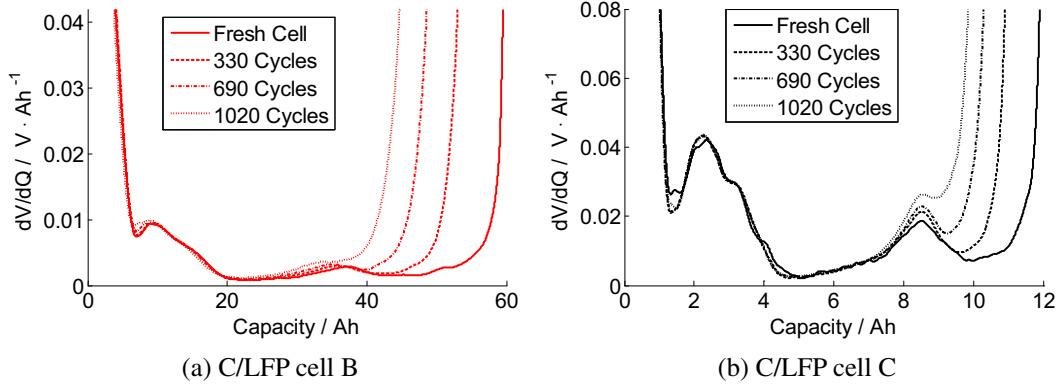
Fig. 9. Differential voltage plot of the full cell after various cycles. (a) C/LFP cell B; (b) C/LFP cell C.

Suppose the capacity of a battery cathode (i.e. the positive electrode) is C_p and that of the anode (i.e. the negative electrode) is C_n. As shown in Fig. 4, the y value of battery cathode (Li$_y$FePO$_4$) at the beginning of charging is y_0, and the x value of anode is x_0. Thus, after charging capacity Q, the y value of battery cathode can be calculated by the Eq. (5), and the x value of battery anode can be calculated by the Eq. (6). Then, the simulated battery terminal voltage $\tilde{V}$ at a certain moment can be calculated by Eq. (7) [2].

$$y = y_0 - \frac{Q}{C_p} \tag{5}$$

$$x = x_0 + \frac{Q}{C_n} \tag{6}$$

$$\tilde{V} = U_p(y) - U_n(x) + IR \tag{7}$$

Here R represents the battery resistance including Ohmic resistance and polarization resistance.

The current I and battery terminal voltage V of the actual batteries can be measured. Suppose the charge process lasts from t_0 to t_{n-1} and n points are sampled. Given different y_0, x_0, C_p, C_n, and R, the predicted battery terminal voltage $\tilde{V}$ can be calculated as well. Then, the root mean squared error (RMSE) between the simulation and the test results is shown in Eq. (8).

$$RMSE = \frac{1}{n} \sum_{t=t_0}^{t_{n-1}} \left(V(t) - \tilde{V}(t) \right)^2 \tag{8}$$

The optimal $[y_0, x_0, C_p, C_n, R]$ can be determined by means of a genetic algorithm to minimize the RMSE between the predicted voltage value and the actual value.
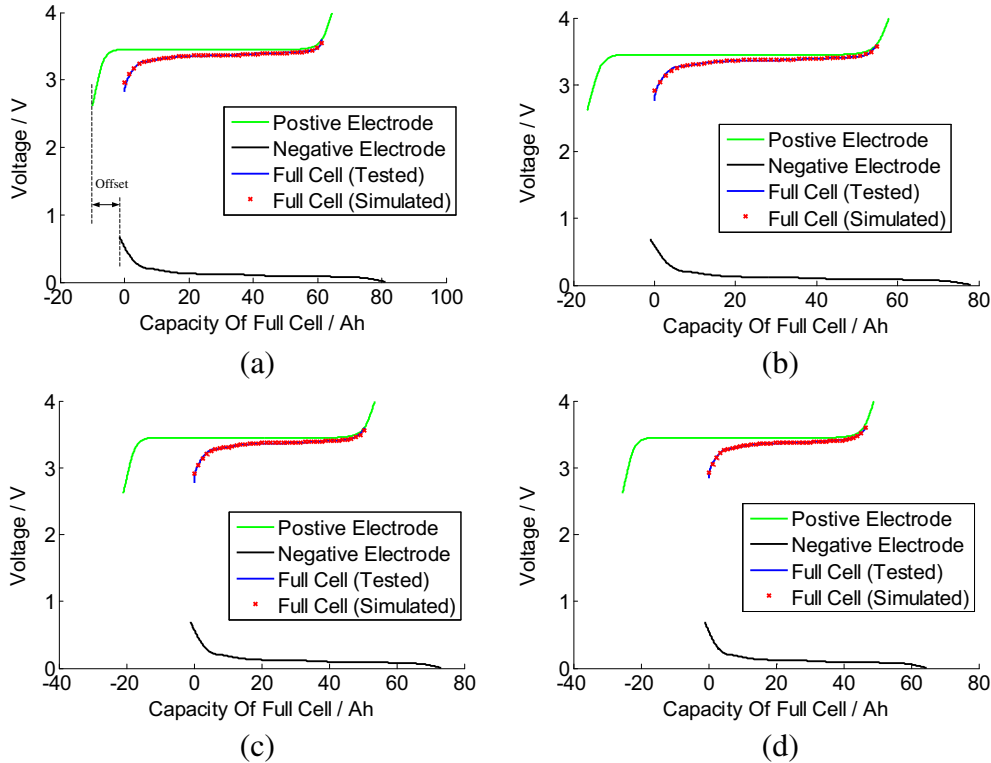

Fig. 10. Simulated (red dots) vs. experimental (blue lines) voltage profiles of full C/LFP cell B after various cycles: (a) fresh cell, (b) after 330 cycles, (c) after 690 cycles, and (d) after 1020 cycles. (For interpretation of the references to color in this figure legend, the reader is referred to the web version of this article.)

A comparison of the simulation and the experimental results of C/LFP cell B are shown in Fig. 10. The charge curves of the battery after different number of cycles can be reproduced using the above method, indicating that it could provide an accurate prediction of the battery internal condition.

The identified result of C/LFP cell B internal parameters is shown in Fig. 11. The evolution of the identified C_p and C_n directly represents the LAM of cathode and anode inside the battery. The changes in R directly represent the changes in the battery resistance. The battery LLI can be generally represented by the offset between the cathode and anode potential curves, as shown in Fig. 10 (a). This offset directly represents the cathode capacity failing to be involved in the insertion and extraction reaction because of the loss of lithium ions. With the increasing cycle number and LLI inside the battery, this offset will become increasingly large, as shown in Fig. 10. Such a definition of LLI is intended for only the test result of LFP cells in this paper. For different lithium-ion batteries, the LLI may be represented in different forms, maybe defined by the capacity of the anode not participating in the reaction at the end of charging. It shall be dealt with flexibly in terms of the actual condition. The offset here can be calculated by Eq. (9).

$$\text{Offset} = (1 - y_0)C_p - x_0C_n \qquad (9)$$

On account of a very small change in C_p, the charge curve starts from SOC $\approx$ 0, and thus, x_0 is negligibly small. Thus, the LLI of LFP batteries here can be investigated through the changes in y_0.

With increase in cycle number, the capacity of the anode C_n consistently decreases, as mentioned in Section 3.1. y_0 also gradually decreases, indicating obvious LLI inside the battery. The resistance of the battery increases slightly. The capacity of battery cathode C_p and x_0 show little change. This also verifies the battery aging mechanism previously estimated with the IC curves. The RMSE between the voltage data obtained from simulation and experiment is lower than approximately 2—5 mV.

Similarly, the simulation result of C/LFP cell C is shown in Fig. 12, and the identified battery internal parameters are shown in Fig. 13. Thus, y_0 also gradually decreases as the cycle number increases, indicating obvious LLI inside the battery, which leads to capacity fade. This also verifies the battery aging mechanism previously estimated with the IC curves. The capacity of the battery anode C_n shows only minor aging; the resistance of the battery increases slightly; the capacity of battery cathode C_p shows little changes, and x_0 changes little. The RMSE between the voltage data obtained from simulation and experiment is lower than 8 mV.

For LFP batteries, such a method may reproduce the battery constant current charge curve precisely, meanwhile identify the battery aging mechanism in terms of the changes in the internal parameter, and then the battery SOH can be better estimated. Furthermore, even if the charge curves are incomplete, this method can also be used to determine the aging mechanism. The genetic algorithm is difficult to implement online because of the massive computational power required. Although it is possible to realize by using methods such as cloud computing, it is very difficult to apply it to the actual BMS. Therefore, further research is required to
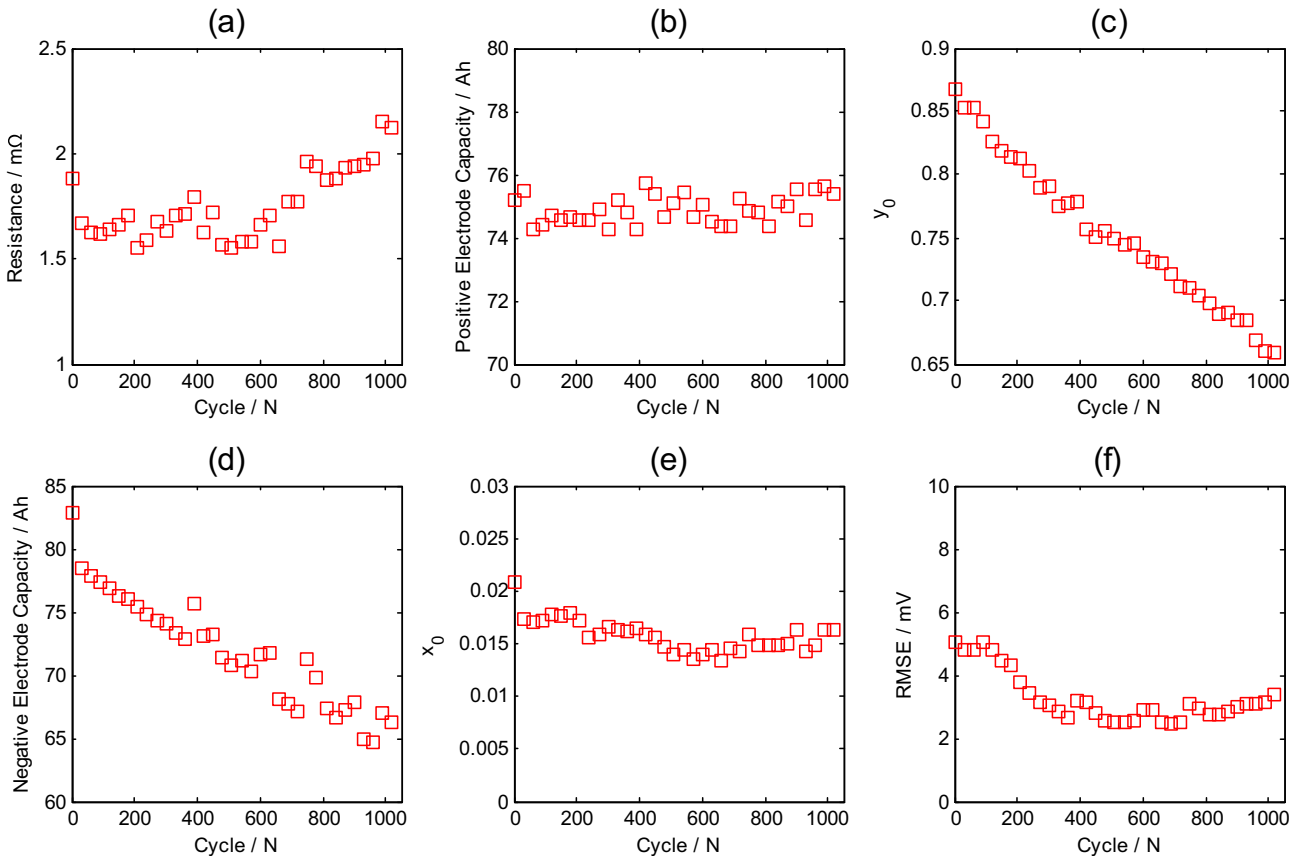

Fig. 11. Evolution of internal parameters of C/LFP cell B, which cause battery aging. (a) resistance, (b) positive electrode capacity, (c) y_0, (d) negative electrode capacity, (e) x_0, and (f) RMSE of the simulation.
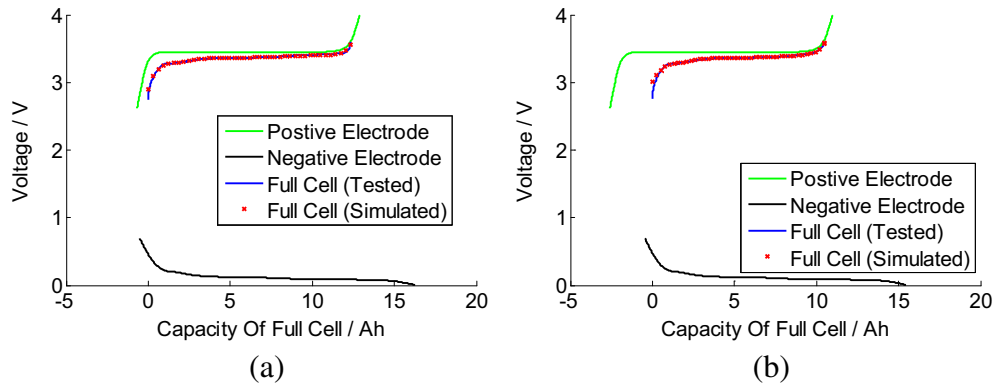
Fig. 12. Simulated (red dots) vs. experimental (blue lines) voltage profiles of full C/LFP cell C after various cycles: (a) fresh cell, (d) after 1020 cycles. (For interpretation of the references to color in this figure legend, the reader is referred to the web version of this article.)

improve such an algorithm for further applying to an on-board BMS.

3.3. On-board analysis of battery aging mechanism

The battery aging mechanism analysis detailed in Section 3.2 is only suitable for off-line analysis, as discussed. For a real BMS in a vehicle, other simpler methods shall be considered to rapidly analyze internal aging conditions of the battery.

The battery DV curves require derivation of the constant current charging voltage curves. Direct difference tends to produce a large amount of noise because of sampling precision, and such methods using curve fitting or smoothing require significant computation. On-board batteries start charging from an uncertain point, which means in the process of charging, it probably starts from higher SOC. Therefore, large changes in peak positions are observed on the DV curves. However, the voltage of a battery has a definite position; thus, the peak positions on the IC curves will not change. It is possible to use the DV curves; however, using the IC curves is better because they can be easily obtained using the point counting method. Therefore, in this study, the battery IC curve is considered for on-board analysis of the battery aging mechanism in BMS.
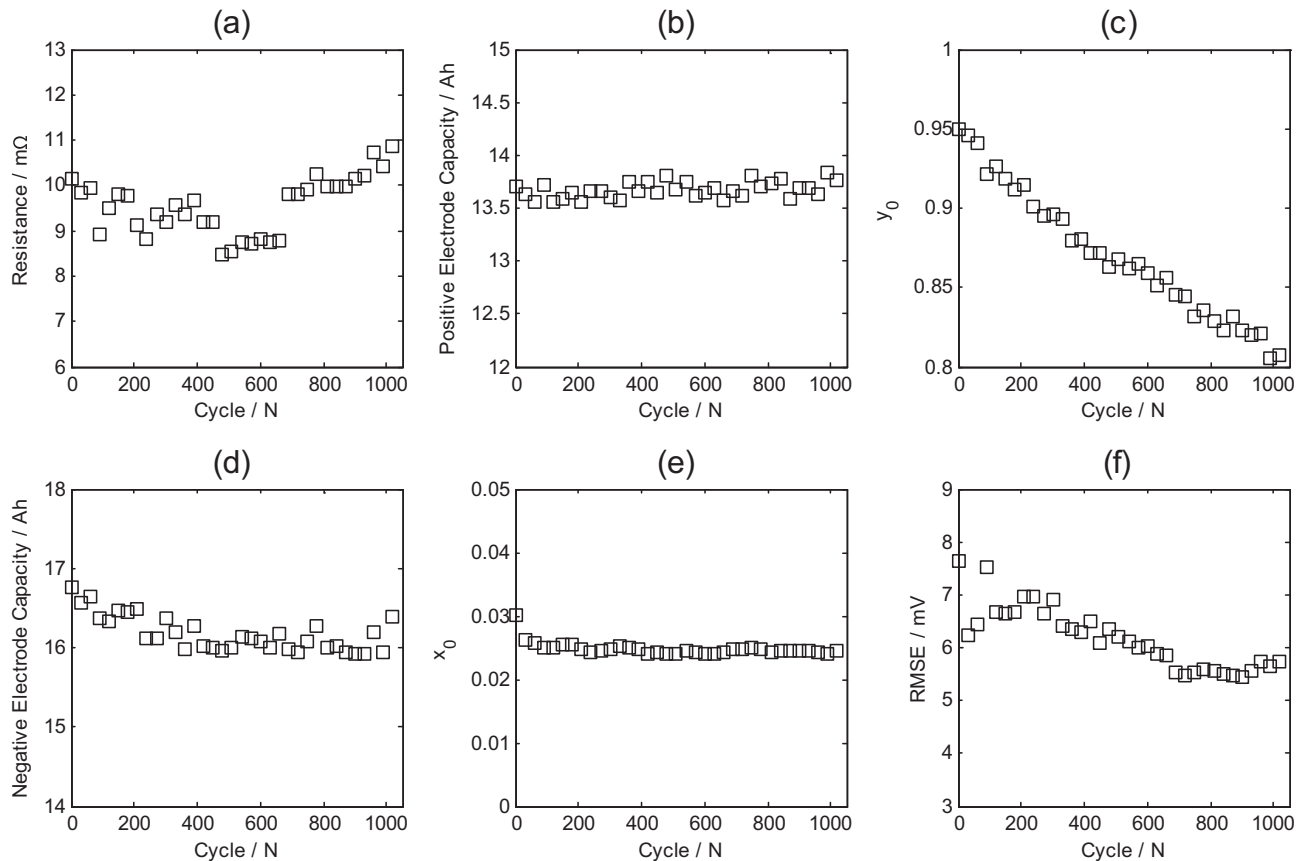

Fig. 13. Evolution of internal parameters of C/LFP cell C, which cause battery aging. (a) resistance, (b) positive electrode capacity, (c) y_0, (d) negative electrode capacity, (e) x_0, and (f) RMSE of the simulation.

The point counting method is used to obtain the IC curve. Consider that the voltage measurement resolution and precision of the on-board BMS are different because of the cost and other reasons. For some low-cost BMS, the possible sampling precision is only 5 mV. Therefore, the width of the voltage interval is selected to be 10 mV. It is clear that a wider interval may lead to a smoother result, but possibly fail to identify the peaks of the IC curves, whereas a narrower interval may possibly suffer major noise causing problems for further analyses. Thus, it can be very convenient and effective to smoothly obtain the battery IC curves by the point counting method. Only small computational power is required; thus, this method can be easily applied to a BMS, and there will be no need to consider such problems as filtering and data smoothing.

The IC curve of C/LFP cell B obtained by means of such point counting method is shown in Fig. 14 and compared with the actual IC curve, from which it can be seen that the three peaks in the IC curves can be identified clearly. The positions of the voltage plateaus in the process of charging can be marked in terms of the voltage positions where the peaks are located on the IC curve. For LFP cells, if the BMS monitors increasing voltage peak positions, it indicates that the resistance of batteries is likely to increase. The battery resistance can also be obtained using methods such as the least square method based on the battery model and the measured battery voltage and current under dynamic working conditions [38]. This result will be more accurate, and therefore it is always not necessary to determine the battery resistance by analyzing the charging voltage curves.

As mentioned previously, the area of each peak represents the capacity participating in the related phase transformation process in the battery charging–discharging process. Therefore, if a simple method rapidly measures the capacity participating in each phase transformation process during the charging process, the on-board diagnosis of the internal aging mechanism of battery becomes convenient and rapid. Considering that the three peaks are very close and have some overlaps, the membership function (MF) is used by reference to fuzzy logic.

Consider that in the charging process, the capacities corresponding to the three phase transformation processes of the anode are labeled as Q_A, Q_B, and Q_C. The corresponding MFs are μ_A, μ_B, and μ_C, as shown by the blue, red, and black lines, respectively, in Fig. 15. Actually, these can be stored in advance in the BMS to save calculation time. As shown in Fig. 16, the capacity related to each phase transformation process can be easily calculated using Eqs. (10)–(12).

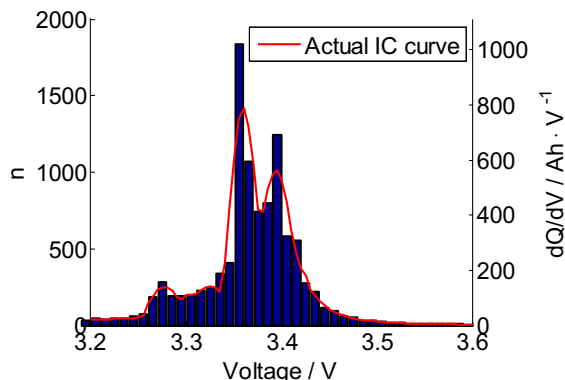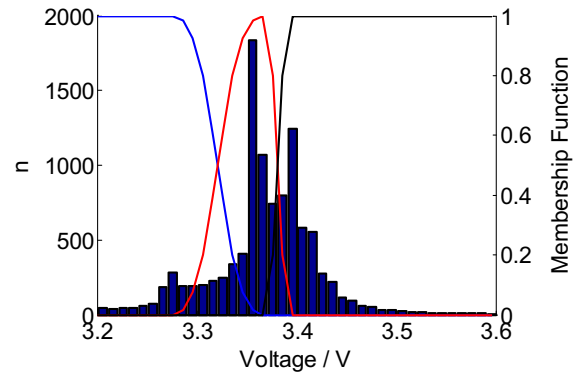$$Q_A = \sum \frac{nI}{3600f} \mu_A = \frac{I}{3600f} \sum n\mu_A \qquad (10)$$

Fig. 15. IC curve of the fresh C/LFP cell B and the related membership function.

$$Q_B = \frac{I}{3600f} \sum n\mu_B \qquad (11)$$

$$Q_C = \frac{I}{3600f} \sum n\mu_C \qquad (12)$$

Fig. 17 shows the evolution of Q_A, Q_B, and Q_C of cell B with increasing cycle number. For C/LFP cell B, it is easy to see that as the cycle number increases, Q_A, Q_B, and Q_C decrease significantly. Q_A and Q_B decrease at almost the same rate, indicating that the loss of capacity arises from the loss of graphite anode active material, and Q_C decreases at a rate obviously higher than Q_A and Q_B, indicating LLI exists besides the loss of graphite anode material, and Q_C decreases because there is no sufficient lithium inventory to be intercalated in the graphite anode at the end of charging.

Similarly, the evolution of Q_A, Q_B, and Q_C of C/LFP cell C with increasing cycle number is shown in Fig. 18. For C/LFP cell C, with increasing cycle number, Q_A and Q_B show little change, indicating that there is almost no loss of the graphite anode active material. Q_C decreases, which indicates that LLI exists in the lithium-ion battery, and there is insufficient lithium inventory to be intercalated in graphite anode at the end of charging, resulting in decrease in Q_C and the total battery capacity.

By using such a simple method, BMS can qualitatively on-board analyze the aging of battery conveniently through the constant current charge curves during the battery charging process, obtain the battery aging mechanism, and then correct and optimize the battery management algorithm.
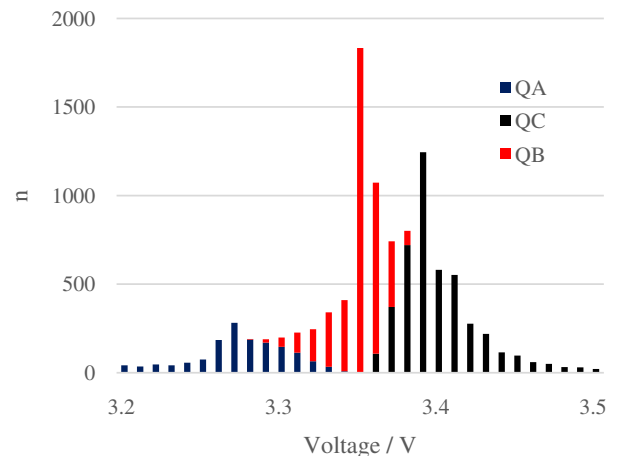
Fig. 14. IC curve of the fresh C/LFP cell B derived by point counting method.

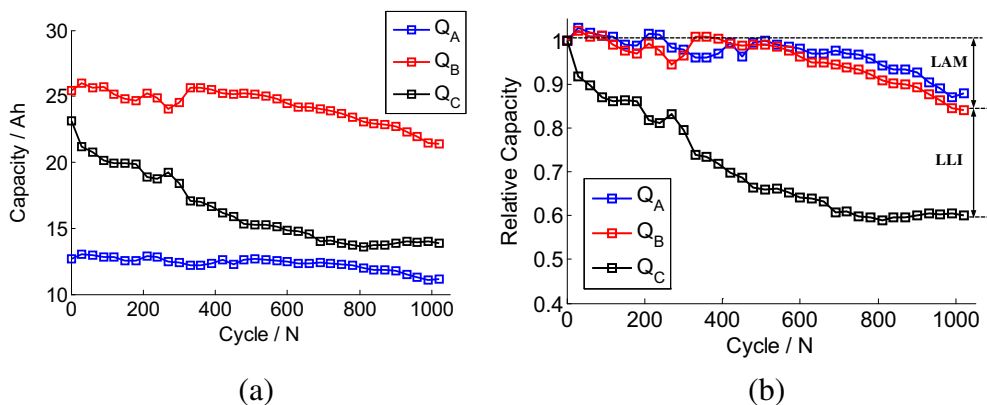Fig. 16. Capacity related to each region.

Fig. 17. Evolution of Q_A, Q_B, and Q_C of C/LFP cell B. (a) capacity, (b) relative capacity.
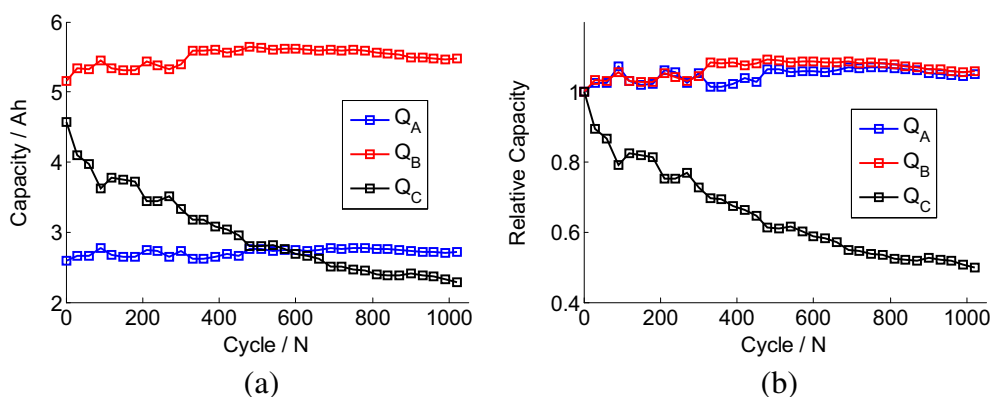

Fig. 18. Evolution of Q_A, Q_B, and Q_C of C/LFP cell C. (a) capacity, (b) relative capacity.

4. LMO Battery aging mechanism

For C/LMO cells D and E, the anode material was graphite, the same as C/LFP cells B and C. The three-phase transformation processes at the anode are also labeled as ①, ②, and ⑤. For the LiMn$_2$O$_4$ cathode, with intercalation of lithium ions, there are two-phase transformations and two corresponding potential plateaus at 4.1 and 3.95 V [39], denoted by I and II.

However, IC curves of C/LMO cells D and E obtained from analysis of the charge curves are shown in Fig. 19. IC curves of the two LMO cells have three obvious peaks. Cell D is dismantled, and the cathode material is used to make a coin cell with Li metal. The constant current charging curve of this coin cell is tested and measured. The charge voltage curve and the IC curve of the coin cell

are shown in Fig. 20. It can be seen that during the insertion/extraction of lithium ions, the cathode material of cell D has three voltage plateaus, indicating that it also has three-phase transformation processes and also three peaks of the IC curve. This demonstrates that the cathode of this commercial LMO cell is not pure LiMn$_2$O$_4$, likely composite cathodes of LMO with LCO-type material, which may lead to the third peak. This test result has also been discussed in our previous paper [34]. Correspondingly, the third peak in Fig. 19 is marked as III.

In terms of the analysis similar to LFP cells introduced in the previous Section 3.1, the IC and DV curves of C/LMO cell D are compared and shown in Fig. 21 for a fresh cell, and cells measured after every 30 cycles up to 240 cycles. For ease of comparison, the related null points of each curve are marked with dotted lines.
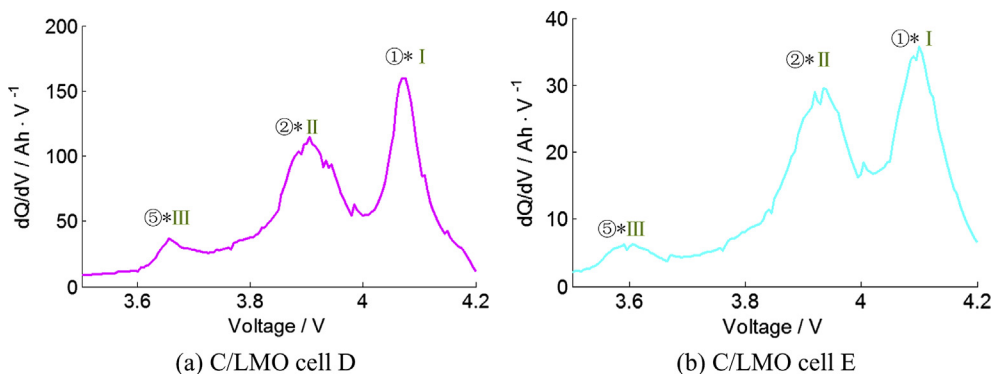

Fig. 19. IC curve of the fresh cell. (a) C/LMO cell D; (b) C/LMO cell E.
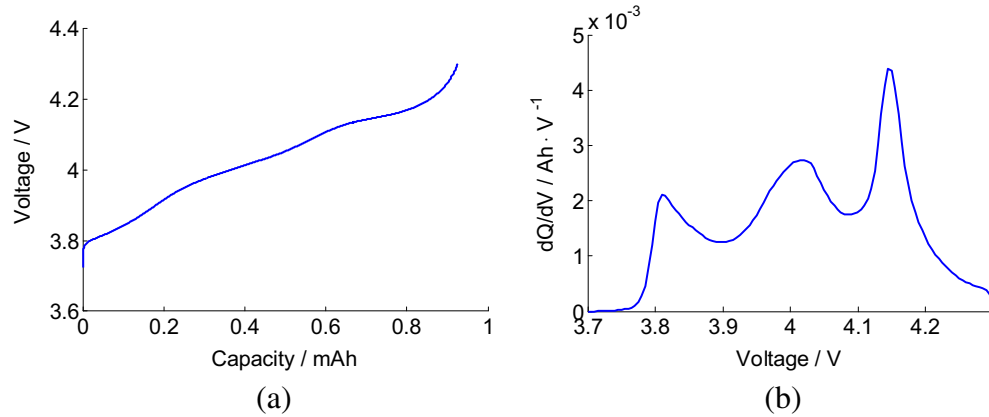
Fig. 20. Charge voltage and IC curve of positive electrode material of C/LMO cell D.

For C/LMO cell D, it can be seen from the IC curve that with increasing cycle number, the voltage positions of the three peaks increase significantly, indicating drastic increase in battery resistance, which is the major reason for performance degradation of cell D. The height of each peak decreases, indicating the LAM of cell D. It should be noticed that no new peaks emerged, and this seems to indicate little differences in the loss rates between the cathode and anode material. After 180 cycles, the battery resistance increases so much that the voltage plateau corresponding to ① *I is higher than the charging cut-off voltage 4.2 V. The related phase transformation process is performed in the constant-voltage charging phase, and thus the peak ① *I disappears from the battery IC curve obtained from the constant current charge curve. The LAM can be verified from the DV curve as well. In the DV curve, Q_A and Q_B decrease, indicating the LAM. There may also be LLI occurring inside the battery; however, it is very difficult to confirm from the IC or DV curves. There is no clear evidence to show that LLI is the major reason of cell D aging. On the whole, the performance degradation of cell D may be a result of increase in resistance, which may be caused by the rapid thickening of the SEI film.

Similarly, the IC and DV curves of C/LMO cell E are compared and shown in Fig. 22, for a fresh cell, and cells measured after every 30 cycles up to 420 cycles. For ease of comparison, the related null points of each curve are also marked with dotted lines.

For C/LMO cell E, it can be seen first from the IC curve that the voltage positions of the three peaks almost had no change, indicating almost no increase in the battery resistance, which is quite different from cell D. The height of each peak decreases substantially, indicating the LAM. Moreover, Peak ⑤*III located at approximately 3.6 V gradually disappears with increasing cycle number, and a new peak, which should correspond to ⑤*II, gradually appears at approximately 3.75 V. This indicates that there is LLI inside the battery [40]. The phase transformation ⑤ of the anode and the phase transformation III of the cathode correspond well with each other in the beginning. They shift from each other with LLI, leading to the disappearance of Peak ⑤*III. With further LLI, ⑤ and II gradually correspond to each other, and Peak ⑤*II appears at a higher voltage of approximately 3.75 V. Simultaneously, the peak corresponding to ① *I in the fresh cell is obviously higher than that to ② *II. With increasing cycle number, the peak corresponding to ① *I degrades at an obviously higher speed than ② *II; the peak of ① *I after 420 cycles is obviously lower than ② *II, and the boundary between the two peaks begins to become blur and a new peak, ② *I, seems to emerge. These phenomena may also be
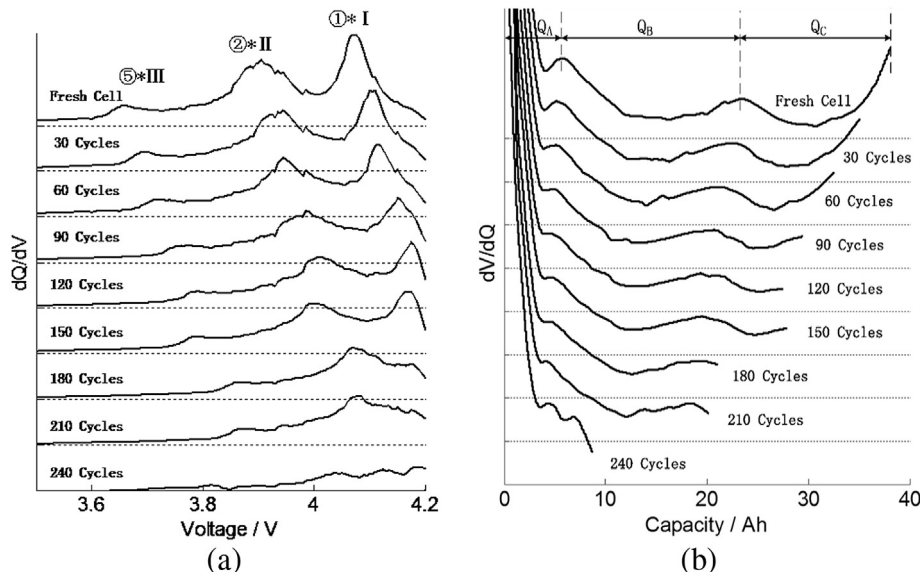

Fig. 21. (a) Incremental capacity and (b) the differential voltage plot of C/LMO Cell D.
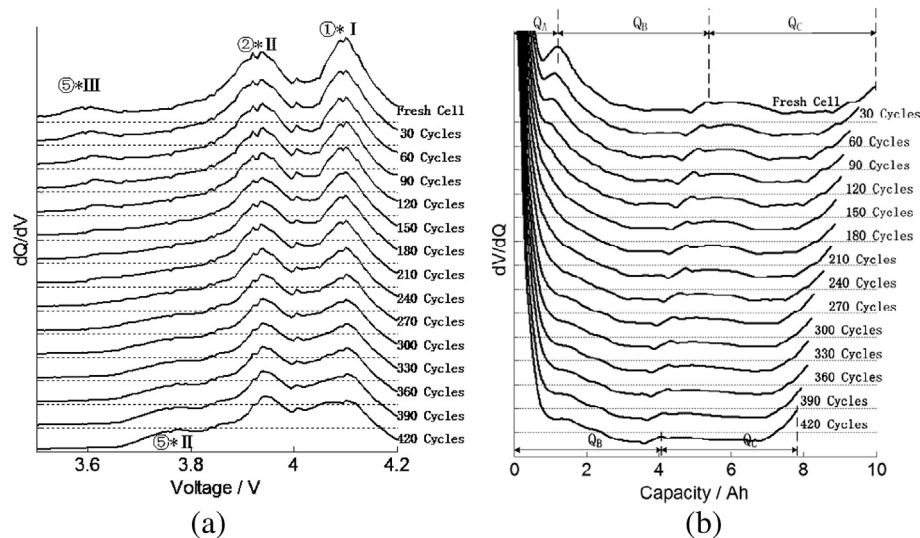
Fig. 22. (a) Incremental capacity and (b) the differential voltage plot of C/LMO Cell E.

explained with LLI. A simple schematic diagram of the LLI of cell E is shown in Fig. 23. It should be noted that this figure simply suggests possible conditions of the cathode and anode when the LLI occurs, and the loss of the cathode and anode active material is not considered. From the DV curve, it can also be seen in Fig. 22 that Q_A roughly marks the capacity corresponding to the reaction III, Q_B indicates the capacity corresponding to reaction II, and Q_C indicates the capacity corresponding to reaction I. With increasing cycle number, Q_A gradually decreases to 0 owing to LLI. With increasing cycle number, Q_B decreases as well, indicating loss of material.

For C/LMO cell D, parameters such as the total capacity of the cathode and anode material after different cycle numbers can be identified by using the genetic algorithm on the basis of the voltage curve of the cathode and anode material. The process is similar to that introduced in Section 3.2. The results are shown in Figs. 24 and 25.

Fig. 24 shows that the major battery aging mechanism is very rapid increase in the battery resistance with increasing cycle number. The cathode and anode active materials also show obvious loss, and there is no obvious LLI. These results can also be quantitatively confirmed from Fig. 25. The battery resistance increases by several orders of magnitude. The cathode and the anode capacity decreases clearly, and it seems that the anode capacity decreases rapidly. x_0 and y_0 (x and y at the start of charging) show nearly no change, indicating that LLI is not the major mechanism of capacity aging.

The cathode material of cell E somewhat differs from that of cell D; by using the voltage curve of cathode material obtained from tests of cell D or from other studies, the constant-current charging curve of cell E cannot be reproduced. This situation is often encountered in real cases. Even if the same type of material is used, the cathode/anode performance of the batteries from different manufacturers is often different owing to differences in the raw materials, manufacturing processes, etc. However, the manufacturer usually objects to dismantle the battery, probably because of technical confidentiality. Hence, we cannot know the specific nature of the cathode material of cell E and cannot perform similar analysis as for cell D. But the major mechanism of battery performance degradation can be analyzed basically by the IC curve, as stated previously.

For LMO batteries, online diagnosis is very difficult to achieve because both the cathode and the anode have three respective voltage plateaus, and the IC curves after different cycle numbers show complex changes. For the LMO batteries actually tested in this paper, the major aging mechanism of cell D is the rapid increase in resistance. In contrast, the loss of cathode material, anode material, and LLI show a smaller influence. The major aging mechanism of cell E is very complex, mainly including the LLI and loss of electrode material. Further research is required for the online diagnosis of LMO batteries.

5. LTO Battery aging mechanism

The anode material of cell A is LTO. For LTO, it is $Li_4Ti_5O_{12}$ in the Li extraction phase and $Li_7Ti_5O_{12}$ in the Li insertion phase. Generally, the anode is basically in the two-phase transformation during the insertion/extraction of lithium ions. There is a voltage plateau at approximately 1.55 V vs. Li/Li$^+$ [30]. The LTO anode is in the abovementioned two-phase transformation region, and the anode potential is located on the voltage plateau, thereby providing a
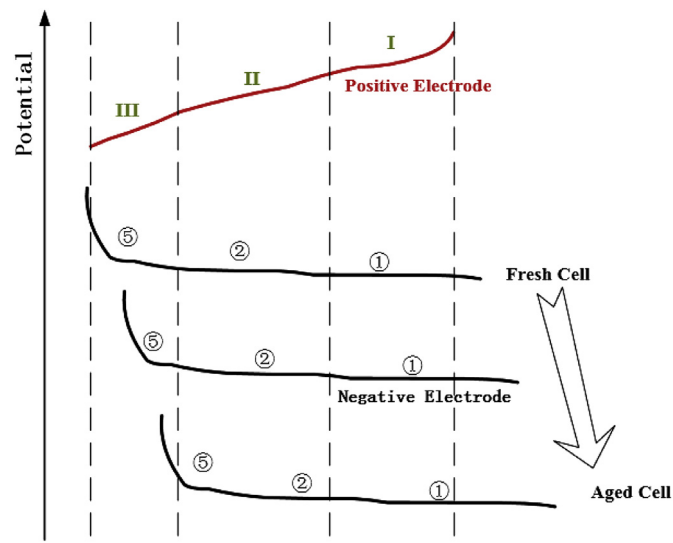

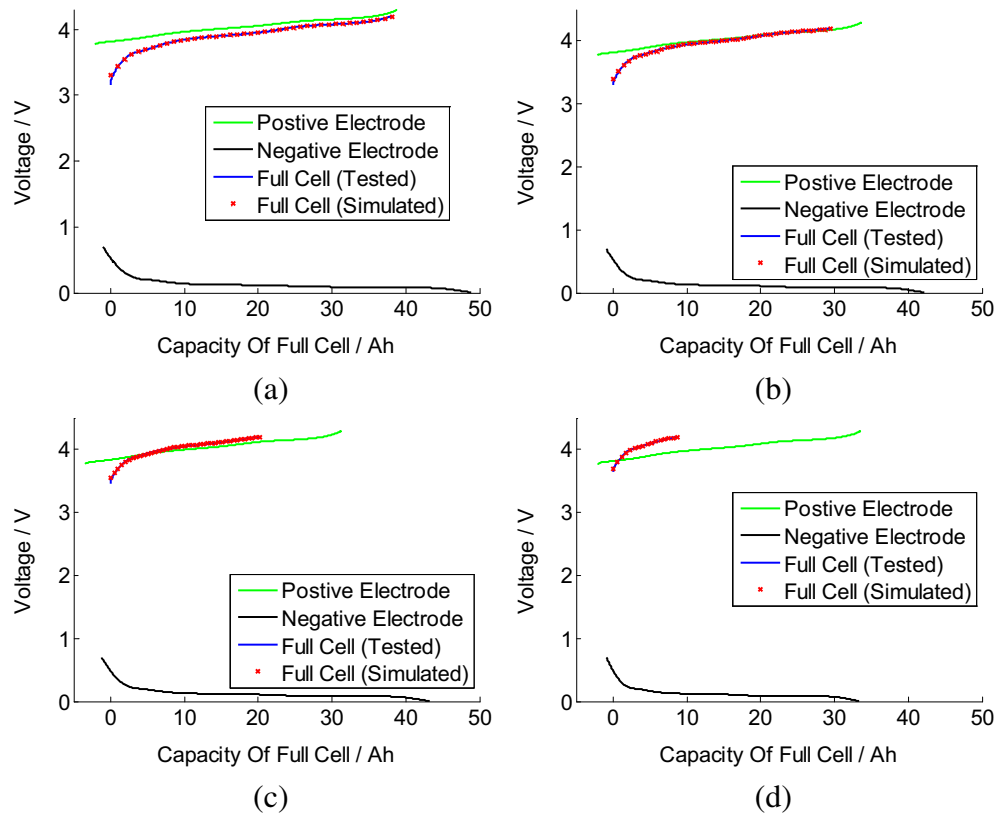**Fig. 23.** Schematics of the influence of LLI of C/LMO cell E.

Fig. 24. Simulated (red dots) vs. experimental (blue lines) voltage profiles of full C/LMO cell D after different cycle numbers: (a) fresh cell, (b) after 90 cycles, (c) after 210 cycles, and (d) after 240 cycles. (For interpretation of the references to color in this figure legend, the reader is referred to the web version of this article.)

reference potential for the cathode reaction. This two-phase transformation region of the anode was labeled as ②. The cathode material of cell A is NCM. Generally, while the battery is charging, for the L333 cathode (LiMn$_{1/3}$Ni$_{1/3}$Co$_{1/3}$O$_2$), with extraction of lithium ions, L333 transforms from a rock salt phase to a hexagonal phase and has a potential plateau at 3.75 V vs. Li/Li+, or 2.2 V vs. LTO. Further Li extraction results in a steady potential increase from 3.75 to 4.2 V in the solid solution region in the hexagonal phase [40]. The IC curve of battery with such NCM material as cathode and LTO anode should have one peak. However, as shown in Fig. 26 (a), the IC curve of cell A actually has two peaks. Consequently, the cathode material used for cell A is probably not L333 (possibly some different elements or synthesis steps to the traditional L333 manufacturing process). The two peaks of the IC reflect the two-phase transformation stages of the cathode, which are labeled as I and II, where the one-phase region is denoted as III, as shown in Fig. 26(a).

The DV curve of LTO/NCM cell A is shown in Fig. 26 (b), from which it can be seen that the DV curve has mainly one peak (1), which arises from the cathode and marks phase equilibrium, and the turning point (2), which arises from the cathode as well and shows that the cathode enters from the phase transformation region to the one-phase region. Therefore, the whole battery charging process can be briefly divided into three regions: A, B, and C. Q_A, Q_B, and Q_C represent the capacity charged in the three regions during the constant current charging process.

The evolution of IC and DV curves of LTO/NCM cell A after different cycle numbers is shown in Fig. 27. With increasing cycle number, the positions of each peak do not change, indicating that there is no increase in battery resistance. Peaks ②*II and ②*I decrease, while Peak ②*III increases. From the DV curve, it can also

be seen that Q_A and Q_B decrease significantly, and Q_C increases correspondingly. Finally, the total battery capacity shows little changes. This may have arisen from LAM of the cathode. The possible mechanism is shown in Fig. 28. However, the exact potential of the cathode material cannot be accurately known because the battery manufacturer did not allow us to dismantle the battery. Yet, Fig. 28 qualitatively shows the condition inside cell A according to the potential curve of the LTO electrode [30] and the IC curve of cell A. According to the literature [41], the LTO anode usually shows little changes with increasing cycle number. Usually, when the battery is charged up to a higher SOC and near the charging end, the potential of an LTO anode will decrease rapidly, thus the battery voltage rapidly increases to the charge cut-off voltage. Therefore, in an LTO battery, there will usually be a little more cathode material [18]. The completion of battery charging is determined by the LTO anode. Thus, when the battery is charged, only part of the cathode material participates in the reaction. Although the cathode active material gradually degrades with increasing cycle number, the capacity of the whole battery shows little changes because there is a slight loss of anode material, and the capacity of the LTO anode remains lower than the capacity of the cathode. However, the continuous loss of cathode material will surely lead to a decrease in Q_A and Q_B, the capacity of battery corresponding to regions I and II, and increase in Q_C, the capacity of the battery corresponding to region III.

It can be predicted that with continuous increase in cycle number, after the capacity of the cathode is lower than that of the anode, the total capacity will mainly depend on the cathode capacity. Then, the battery capacity will rapidly decrease with LAM of the cathode. This phenomenon has been confirmed during our LTO batteries cycle life test at 55 °C, and the results will be analyzed and published in future papers.
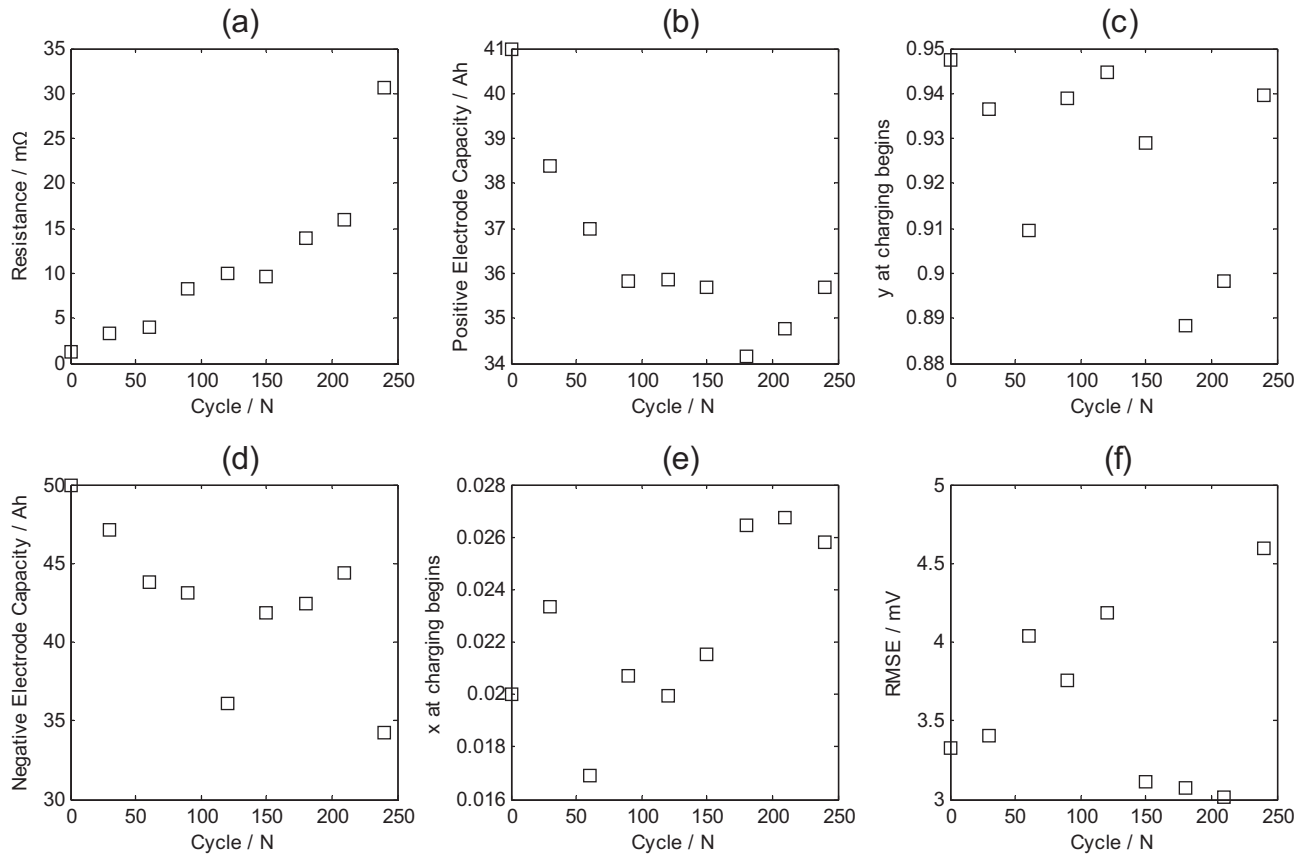
Fig. 25. Evolution of internal parameters of C/LMO cell D which cause battery aging. (a) resistance, (b) positive electrode capacity, (c) y at charging begins, (d) negative electrode capacity, (e) x at charging begins, and (f) the RMSE of the simulation.

As nothing is known about the performance of the electrode material in LTO/NCM cell A owing to confidentiality, we cannot reconstruct the charge curves, as stated in Section 3.2. This is regarded as one of the dilemmas of the current BMS. However, it is believed that this can be solved in the future.

6. Conclusions

Accurate SOH estimation requires on-board analysis of the aging mechanism of lithium-ion batteries. It is very important and

difficult to identify the aging mechanism. This paper is mainly intended to use simple non-destructive methods for analyzing the aging mechanisms of batteries. The aging mechanisms of five commercial lithium-ion batteries involved in cycle life testing are analyzed using IC curves, DV curves, and the charge voltage curve reproduction on the basis of the 1/3 C constant current charge curves at 25 °C.

For LTO/NCM cell A, there is almost no loss of battery capacity and LTO anode active material inside the battery, but obvious loss of cathode active material. For C/LFP cell B, the battery aging
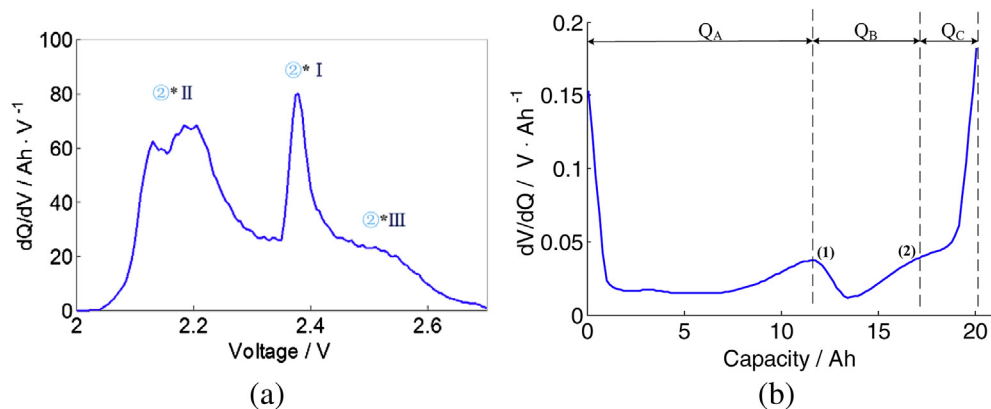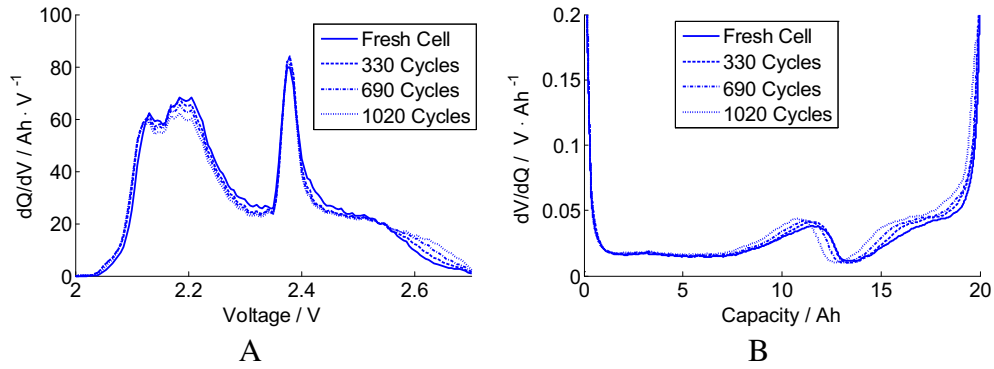

Fig. 26. IC and DV plot of LTO/NCM cell A.

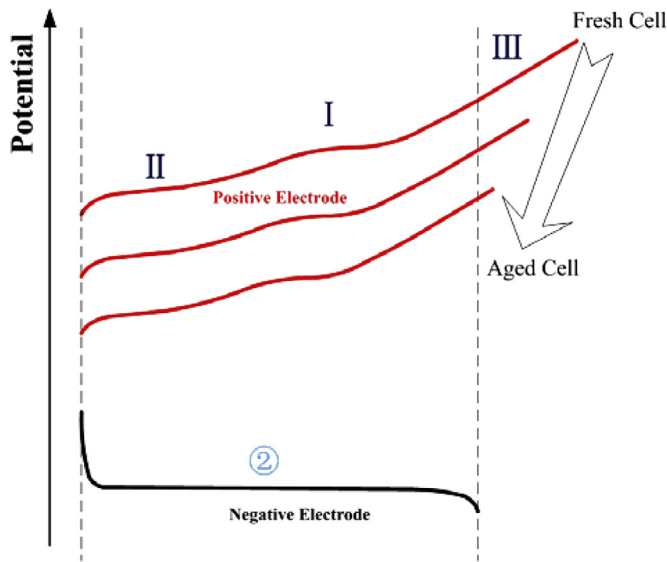**Fig. 27.** Evolution of IC and DV plot of LTO/NCM cell A after different cycles.


Fig. 28. Schematics of internal electrodes potential of LTO/NCM cell A from a fresh cell to an aged cell.

mainly arises from the loss of lithium inventory and loss of the anode active material. For C/LFP cell C, the battery aging mainly arises from loss of lithium inventory, while there was no clear loss of either the cathode or anode active material. For C/LMO cell D, the battery aging mainly arises from the substantial increase in resistance. Meanwhile, there is an obvious loss of active material. For C/LMO cell E, the battery aging mainly arises from the loss of lithium inventory, and there is no obvious loss of active material.

For C/LFP cells, using a simple method, the battery IC curve could be rapidly and easily derived and the battery aging can be analyzed based on the membership function. This method is expected to be successfully implemented in the real vehicle BMS owing to its lower calculating complexity. For C/LMO cells, the aging mechanism is more complicated, and further research is still required to achieve on-board identification of the aging mechanism.

Acknowledgments
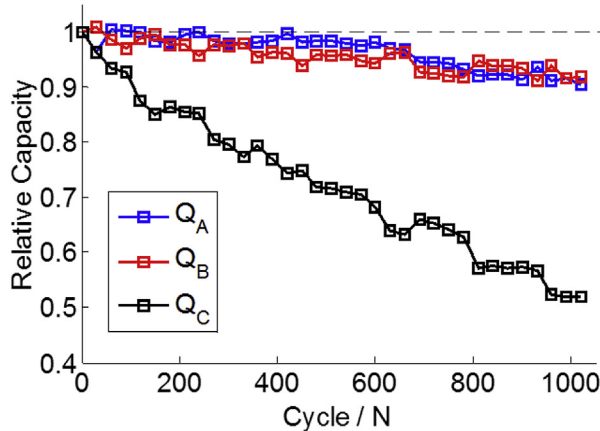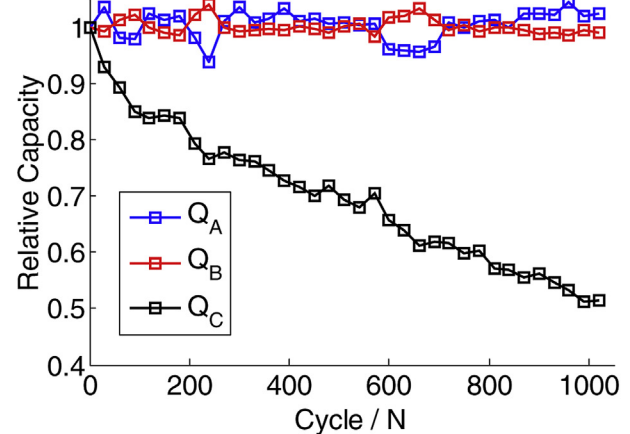
(a) C/LFP cell B

(b) C/LFP cell C

Fig. 29. Manual separation results of Q_A, Q_B, and Q_C, (a) C/LFP cell B, (b) C/LFP cell C.

Appendix A. Abbreviations and nomenclature

BMS	battery management system
C	carbon
DV	differential voltage
EV	electric vehicle
IC	incremental capacity
L333	$LiNi_{1/3}Co_{1/3}Mn_{1/3}O_2$
LAM	loss of active material
LFP	$LiFePO_4$
LLI	loss of lithium inventory
LMO	$LiMn_2O_4$
LTO	$Li_4Ti_5O_{12}$
MF	membership function
NCM	$LiNi_xCo_yMn_{1-x-y}O_2$
RMSE	rooted mean squared error
RPT	reference performance test
SEI	solid electrolyte interface
SEM	scanning electron microscope
SOC	state of charge
SOF	state of function
SOH	state of health
SOS	state of safety
XRD	X-ray diffraction
p	water pressure
ρ	water density
g	gravitational acceleration
h	water height
Q	water quantity/capacity
A	sectional area
f	sampling frequency
V	cell voltage
$\tilde{V}$	simulated cell voltage
R	battery resistance
I	current
x	Li concentration of negative electrode
y	Li concentration of positive electrode
C_p	capacity of positive electrode
C_n	capacity of negative electrode
Q_A, Q_B, Q_C	capacity related to the different phase transformation processes

Appendix B. On-board analysis of battery aging mechanism

Currently most methods which deal with the battery aging mechanism are post mortem methods. How to identify the battery aging mechanism on-board simply and efficiently is still a challenge for the BMS in EV.

If the capacity corresponding to each peak of the IC curve could be calculated in the BMS, the BMS could on-board analyze the battery aging mechanism. However, because of the massive computational power required, methods like genetic algorithm is quite difficult to be implemented online. And consider the limited measurement resolution, the IC curve derived in BMS is quite rough and it is hard to tell which parts corresponding to which peak. Using the method introduced in Section 3.3, after carefully chosen the MF according to the experiment results, with the Eqs. (10)–(12), the separation results could be directly and easily derived, no matter how complicated the peak shapes are. Even the peak vanishes, the BMS could calculate a results.

The manual separation of the 3 section and Q_A, Q_B, and Q_C determination according to the DV curves is shown in Fig. 29. It could be found that in Fig. 7 that with battery gradually ages, the peak ① *II eventually vanishes and it is very hard to distinguish it from the peak ② *II, thus here the DV curve is used to separate the capacity by hand.

The results shown in Figs. 17 and 18 which is derived by MF are just similar to the results shows in the Fig. 29. That validate that this method could qualitatively determine the battery aging mechanism and could be used in the BMS. And we believe this method has the potential to semi-quantitatively analyze the aging mechanism of the battery.

The key problem of this method is to find the appropriate MF. In the Section 3.3, the used MF is chosen according to the experiment results of LFP cells. Since there are only three peaks of the LFP battery IC curve, the MF is not complicated. For batteries whose resistance increase dramatically, the MF should be shifted according to the peak position change. For batteries with more peaks, complicated MF should be carefully chosen according to the battery performance.

References

[1] L.G. Lu, X.B. Han, J. Li, J. Hua, M. Ouyang, J. Power Sources 226 (2013) 272–288.
[2] M. Dubarry, C. Truchot, B.Y. Liaw, J. Power Sources 219 (2012) 204–216.
[3] J. Neubauer, A. Pesaran, J. Power Sources 196 (2011) 10351–10358.
[4] I. Bloom, J.P. Christophersen, D.P. Abraham, K.L. Gering, J. Power Sources 139 (2005) 295–303.
[5] K. Honkura, K. Takahashi, T. Horiba, J. Power Sources 196 (2011) 10141–10147.
[6] H.M. Dahn, A.J. Smith, J.C. Burns, D.A. Stevens, J.R. Dahn, J. Electrochem. Soc. 159 (2012) A1405–A1409.
[9] B. Scrosati, J. Garche, J. Power Sources 195 (2010) 2419–2430.
[10] T.F. Yi, L. Jiang, J. Shu, C. Yue, R. Zhu, H. Qiao, J. Phys. Chem. Solids 71 (2010) 1236–1242.
[11] E. Peled, J. Electrochem. Soc. 126 (1979) 2047.
[12] P. Verma, P. Maire, P. Novák, Electrochim. Acta 55 (2010) 6332–6341.
[13] D. Aurbach, J. Power Sources 89 (2000) 206–218.
[14] D. Aurbach, E. Zinigrad, Y. Cohen, H. Teller, Solid State Ionics 148 (2002) 405–416.
[15] J. Vetter, P. Novák, M.R. Wagner, C. Veit, K.C. Möller, J.O. Besenhard, M. Winter, M. Wohlfahrt-Mehrens, C. Vogler, A. Hammouche, J. Power Sources 147 (2005) 269–281.
[16] M. Koltypin, Y.S. Cohen, B. Markovsky, Y. Cohen, D. Aurbach, Electrochem. Commun. 4 (2002) 17–23.
[17] T. Ohzuku, A. Ueda, N. Yamamoto, J. Electrochem. Soc. 142 (1995) 1431.
[18] W. Lu, J. Liu, Y.K. Sun, N. Amine, J. Power Sources 167 (2007) 212–216.
[19] A.D. Pasquier, C.C. Huang, T. Spitler, J. Power Sources 186 (2009) 508–514.
[20] X. Li, Y. Xu, C. Wang, J. Alloys Compd. 479 (2009) 310–313.
[21] K.Y. Chung, K.B. Kim, Electrochim. Acta 49 (2004) 3327–3337.
[22] P. Lucas, C.A. Angell, J. Electrochem. Soc. 147 (2000) 4459–4463.
[23] R.J. Gummow, A. de Kock, M.M. Thackeray, Solid State Ionics 69 (1994) 59–67.
[24] K. Amine, J. Liu, I. Belharouak, S.H. Kang, I. Bloom, D. Vissers, G. Henriksen, J. Power Sources 146 (2005) 111–115.
[25] I. Belharouak, G.M. Koenig Jr., K. Amine, J. Power Sources 196 (2011) 10344–10350.
[26] J.M. Kim, H.T. Chung, Electrochim. Acta 49 (2004) 937–944.
[27] Y. Huang, J. Chen, J. Power Sources 188 (2009) 538–545.
[28] K.M. Shaju, G.V.S. Rao, B.V.R. Chowdari, Electrochim. Acta 48 (2002) 145–151.
[29] W.J. Zhang, J. Power Sources 196 (2011) 2962–2970.
[30] K. Zaghib, M. Dontigny, J. Power Sources 196 (2011) 3949–3954.
[31] M. Dubarry, V. Svoboda, Electrochem. Solid-State Lett. 9 (2006) A454–A457.
[32] M. Dubarry, B.Y. Liaw, J. Power Sources 196 (2011) 3420–3425.
[33] M. Dubarry, B.Y. Liaw, J. Power Sources 194 (2009) 541–549.
[34] X. Feng, J. Li, M. Ouyang, L. Lu, J. Li, X. He, J. Power Sources 232 (2013) 209–218.
[35] M. Kassem, J. Bernard, R. Revel, S. Pélissier, F. Duclaud, C. Delacourt, J. Power Sources 208 (2012) 296–305.
[36] M. Kassem, C. Delacourt, J. Power Sources 235 (2013) 159–171.
[37] E. Prada, D. Di Domenico, Y. Creff, J. Bernard, V. Sauvant-Moynot, F. Huet, J. Electrochem. Soc. 159 (2012) A1508–A1519.
[38] Y. Zheng, M. Ouyang, L. Lu, J. Li, X. Han, L. Xu, J. Power Sources 223 (2013) 136–146.
[39] M. Dubarry, C. Truchot, M. Cugnet, B.Y. Liaw, K. Gering, S. Sazhin, D. Jamison, C. Michelbacher, J. Power Sources 196 (2011) 10328–10335.
[40] M. Dubarry, C. Truchot, B.Y. Liaw, K. Gering, S. Sazhin, D. Jamison, C. Michelbacher, J. Power Sources 196 (2011) 10336–10343.
[41] Z. Yu, X. Zhang, G. Yang, J. Liu, J. Wang, R. Wang, J. Zhang, Electrochim. Acta 56 (2011) 8611–8617.